The Journal of Engineering

The 7th International Conference on Renewable Power Generation (RPG 2018)

IET Journals
The Institution of Engineering and Technology

Combined source-effect of photovoltaic generator and bi-directional dc–dc battery charger on inverter control dynamics

eISSN 2051-3305
Received on 30th October 2018
Accepted on 10th January 2019
E-First on 1st July 2019
doi: 10.1049/joe.2018.9332
www.ietdl.org

Roosa-Maria Sallinen[1] ✉, *Tuomas Messo*[1]

[1]*Laboratory of Electrical Energy Engineering, Tampere University, Tampere, Finland*

✉ *E-mail: roosa-maria.sallinen@tuni.fi*

Abstract: This study presents a method to solve the dynamic model of a grid-connected photovoltaic (PV) inverter with battery energy storage. A three-phase grid-connected solar-battery system is studied using small-signal state-space modelling in the synchronously rotating *dq*-reference frame. The combined effect of a PV generator and a bi-directional dc–dc battery charger (BC) on the inverter dynamic behaviour is analysed. It is shown that the characteristic right-half-plane pole in the PV inverter's dc-link voltage control dynamics shifts to a lower frequency when the BC is connected, which improves the stability of the system and allows a lower bandwidth for the dc-link voltage control.

1 Introduction

In recent years, different hybrid renewable-energy sources (RESs) have been increasingly researched and developed worldwide. The hybrid solutions aim to complement each other's weaknesses resulting in more efficient and reliable energy sources as a whole. Many types of RESs, such as photovoltaic (PV) generators, have an intermittent nature due to changing environmental factors, such as irradiation levels and temperature. Thus, predicting and controlling the energy production of these sources is more difficult compared to traditional power sources with the inertial response, such as gas turbines. As a result, these intermittent energy sources increase the overall need for regulated power reserve to keep the total production in balance with the consumption [1, 2].

To this end, battery energy storage systems (BESSs) are considered a good addition to PV generators (PVGs) and other intermittent sources due to their fast response time, reliable technology, and increasing cost-efficiency [3, 4]. The main idea of solar-battery systems is to utilise the batteries to store any excess solar energy to offer the stored energy during low irradiation levels, for example during night-time. In [5], BESS was employed for smoothing the PV power fluctuations under variations in solar irradiance. BESS can also be used for arbitrage [6], in which the charging and discharging of the BESS is chosen based on the current electricity price. Thus, there exist several promising applications for grid-connected solar-battery systems.

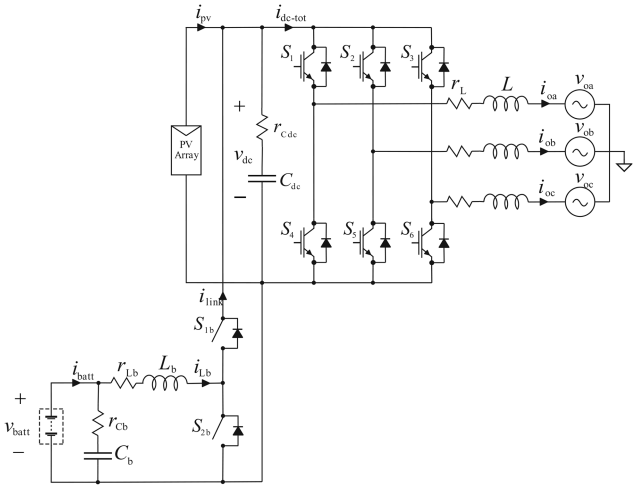

Fig. 1 *Layout of the grid-connected solar-battery system*

However, grid-connected solar-battery systems are difficult to model due to the number of different subsystems, power electronic converters and their controllers, and the variety of operating modes. The system consists of multiple different subsystems: BESS and its charge regulator (battery charger (BC)), PVG, and inverter and its output filters. The battery can be charged, discharged, or disconnected. The charging and discharging of the battery can be achieved by controlling the current and/or the voltage of the battery, depending on the chosen battery technology and its state of charge (SOC). The PVG is functioning either in the constant current region (CCR), constant voltage region (CVR) or at its maximum power point (MPP), which changes the dynamics of the PVG profoundly, as discussed in [7].

Since the stability of a power converter can be affected significantly by its operating condition, the studied system should be examined at all possible operating points. Furthermore, even though all the subsystems are stable and perform well within their own nominal operational ranges when integrated as a whole, the system may become unstable due to unexpected interactions among the subsystems. An accurate small-signal model is required to necessitate reliable controller design to guarantee the stability of the converter under varying control modes and operating points.

The effect of a PVG on the inverter dynamics has been studied previously in [7]. Bi-directional dc–dc converters have been modelled and their stability assessed in, e.g. [8, 9]. To study the dynamic behaviour of the whole system, this paper presents a small-signal model of the grid-connected solar-battery system, which can be used to analyse how the BC (i.e. bi-directional dc–dc converter) and the PVG affect the inverter dynamics. As a result, the effect of the PVG and the BESS can be taken into account in the inverter control design to guarantee stable and robust performance. Frequency domain results of the studied system under various operating conditions are presented to verify the dynamic model.

2 System configuration

Fig. 1 shows the configuration of the system under consideration: a three-phase PV inverter with a BESS connected at the dc-link through a bi-directional dc–dc converter. The dc–dc converter functions as the BC by controlling the battery current, enabling both charging and discharging modes. Note, that the battery voltage control is not considered in this paper. The inverter is connected to the grid through an L-filter.

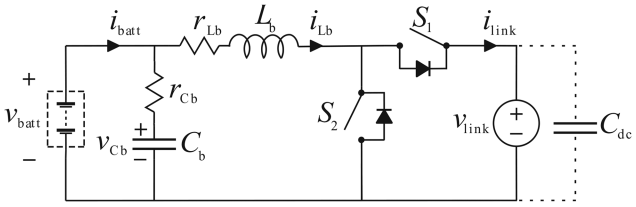

Fig. 2 *Bi-directional dc–dc converter*

2.1 Dynamic model of BC

Fig. 2 shows the schematic diagram of the bi-directional dc–dc converter for connecting the battery storage to the common dc link. Only one of the switches is active (i.e. switching) at a time: S2 when discharging (boost mode) and S1 when charging (buck mode). Note that the direction of the current in the figure is as in discharging mode; in charging mode, the flow would be the opposite. A proportional–integral (PI) controller is used to regulate the current of the BESS.

The linearised state-space representation of the BC is given in (1), where

$$R_{eq} = (r_{Lb} + r_d)(D-1) - D(r_{Lb} + r_{sw})$$
$$V_{eq} = V_d + V_{link} + I_{Lb}(r_d + r_{sw}),$$

r_{sw} and r_d are the parasitic resistances of the switches and the diode, respectively, and V_d is the voltage drop over the diode when set in the forward direction. The rest of the variables are given in Fig. 2 and D_{eq} is defined as $1-D_2$ while discharging the battery and as D_1 while charging the battery. Also, the upper signs of the plus-minus–pairs are for the discharging mode and lower signs for the charging mode. (see (1)) The transfer functions from the input variables to the output variables at open loop can be solved in the frequency-domain by utilising

$$\boldsymbol{Y}(s) = \left(\boldsymbol{C}(s\boldsymbol{I} - \boldsymbol{A})^{-1}\boldsymbol{B} + \boldsymbol{D}\right)\boldsymbol{U}(s) \tag{2}$$

where the matrices $\boldsymbol{A}$, $\boldsymbol{B}$, $\boldsymbol{C}$, $\boldsymbol{D}$, $\boldsymbol{Y}$, and $\boldsymbol{U}$ are as dictated in (1) and $\boldsymbol{I}$ is the unity matrix. As a result, the open-loop dynamics can be presented in matrix form as

$$\begin{bmatrix} \hat{i}^{bc}_{batt} \\ \hat{i}^{bc}_{link} \end{bmatrix} = \begin{bmatrix} Y^{bc}_{in-o} & T^{bc}_{oi-o} & G^{bc}_{ci-o} \\ G^{bc}_{io-o} & -Y^{bc}_{o-o} & G^{bc}_{co-o} \end{bmatrix} \begin{bmatrix} \hat{v}^{bc}_{batt} \\ \hat{v}^{bc}_{link} \\ \hat{i}^{bc}_{batt-ref} \end{bmatrix}, \tag{3}$$

where the 2×3 matrix consists of the transfer functions between the input and the output variables. Consecutively, by utilising feedback control from the battery current, the closed-loop dynamics can be presented as

$$\begin{bmatrix} \hat{i}^{bc}_{batt} \\ \hat{i}^{bc}_{link} \end{bmatrix} = \begin{bmatrix} Y^{bc}_{in-c} & T^{bc}_{oi-c} & G^{bc}_{ci-c} \\ G^{bc}_{io-c} & -Y^{bc}_{o-c} & G^{bc}_{co-c} \end{bmatrix} \overbrace{\begin{bmatrix} \hat{v}^{bc}_{batt} \\ \hat{v}^{bc}_{link} \\ \hat{i}^{bc}_{batt-ref} \end{bmatrix}}^{U_{bc}} \tag{4}$$

which is equal to (see (5)) . Moreover, the input control loop-gain is expressed as

$$L_{in-bc} = G^{bc}_{PI} G^{bc}_{ci-o} \tag{6}$$

Note, that different switches are controlled in the charging and discharging modes while the un-active switch is set to open. Furthermore, the direction of the current needs to be taken into account in the controller to make the system stable in both operating modes.

2.2 Dynamic model of PVG

The amount of current PVG can produce at a certain voltage level is correlated with the irradiance level. The PV cells are often modelled using the one-diode model presented in Fig. 3. According to the model, the current produced by the PV cell can be expressed as

$$i_{pv-cell} = i_{ph} - \underbrace{i_o\left[\exp\left(\frac{v_{pv} + r_s i_{pv}}{A v_t}\right)\right]}_{i_d} - \frac{v_{pv} + r_s i_{pv-cell}}{r_{sh}} \tag{7}$$

where i_{ph} is the light generated current, i_o the dark saturation current of the cell, v_{pv} the voltage across the cell, r_s the parasitic series resistance, r_{sh} the shunt resistance, A the ideality factor, and $v_t = kT/q$ the thermal voltage of the cell, where k is the Boltzmann constant, q the elementary charge, and T the temperature. Finally, i_d presents the diode resistance.

The PVG consists of multiple PV modules, which are built from multiple PV cells. When the PVG operates under uniform

$$\begin{bmatrix} \frac{d\hat{v}^{bc}_{Cb}}{dt} \\ \frac{d\hat{i}^{bc}_{Lb}}{dt} \end{bmatrix} = \overbrace{\begin{bmatrix} -\frac{1}{C_b r_{Cb}} & 0 \\ 0 & \frac{R_{eq}}{L_b} \end{bmatrix}}^{A} \begin{bmatrix} \hat{v}^{bc}_{Cb} \\ \hat{i}^{bc}_{Lb} \end{bmatrix} + \overbrace{\begin{bmatrix} \frac{1}{C_b r_{Cb}} & 0 & 0 \\ \pm\frac{1}{L_b} & \mp\frac{D_{eq}}{L_b} & \frac{V_{eq}}{L_b} \end{bmatrix}}^{B} \overbrace{\begin{bmatrix} \hat{v}^{bc}_{batt} \\ \hat{v}^{bc}_{link} \\ \hat{d}^{bc}_{1/2} \end{bmatrix}}^{U}$$
$$\overbrace{\begin{bmatrix} \hat{i}^{bc}_{batt} \\ \hat{i}^{bc}_{link} \end{bmatrix}}^{Y} = \overbrace{\begin{bmatrix} \mp\frac{1}{r_{Cb}} & 1 \\ 0 & D_{eq} \end{bmatrix}}^{C} \begin{bmatrix} \hat{v}^{bc}_{Cb} \\ \hat{i}^{bc}_{Lb} \end{bmatrix} + \overbrace{\begin{bmatrix} \pm\frac{1}{r_{Cb}} & 0 & 0 \\ 0 & 0 & \mp I_{Lb} \end{bmatrix}}^{D} \begin{bmatrix} \hat{v}^{bc}_{batt} \\ \hat{v}^{bc}_{link} \\ \hat{d}^{bc}_{1/2} \end{bmatrix} \tag{1}$$

$$= \begin{bmatrix} \frac{Y^{bc}_{in-o}}{1+L_{in-bc}} & \frac{T^{bc}_{oi-o}}{1+L_{in-bc}} & \frac{L_{in-bc}}{1+L_{in-bc}} \\ G^{bc}_{io-o} - \frac{G^{bc}_{co-o}G^{bc}_{PI}Y^{bc}_{in-o}}{1+L_{in-bc}} & -\left(Y^{bc}_{o-o} - \frac{G^{bc}_{co-o}G^{bc}_{PI}T^{bc}_{oi-o}}{1+L_{in-bc}}\right) & \frac{G^{bc}_{co-o}G^{bc}_{PI}}{1+L_{in-bc}} \end{bmatrix} \boldsymbol{U}_{bc}, \tag{5}$$

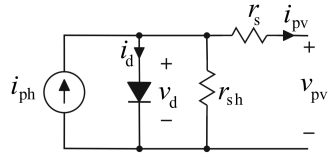

Fig. 3 *PV one-diode model*

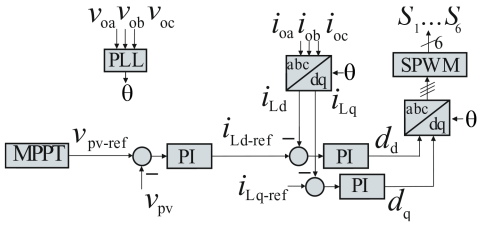

Fig. 4 *Inverter control system*

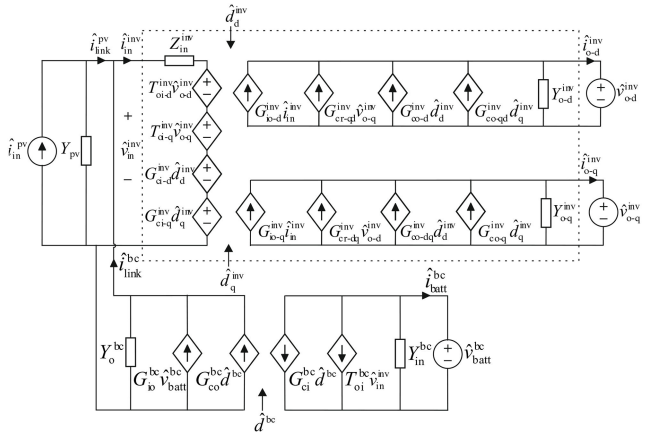

Fig. 5 *Linear equivalent circuit of the BESS-PV inverter*

irradiance, its current–voltage characteristic exhibits a unique point, the maximum power point (MPP), where the PVG produces maximum output power and which location depends on, for example the irradiance level and the cell temperature [10]. Due to the voltage–current characteristics of PVGs, when the PVG voltage is higher than the MPP voltage, the PVG is said to operate in CVR, and when the PVG voltage is lower than the MPP voltage, the PVG is said to operate in CCR. To operate the PVG efficiently, its MPP needs to be tracked continuously to yield the maximum power.

2.3 Dynamic model of grid-connected inverter

The dynamic behaviour of the three-phase inverter can be presented in matrix form as

$$\begin{bmatrix} \hat{v}_{in}^{inv} \\ \hat{i}_{o-d}^{inv} \\ \hat{i}_{o-q}^{inv} \end{bmatrix} = \begin{bmatrix} Z_{in}^{inv} & T_{oi-d}^{inv} & T_{oi-q}^{inv} & G_{ci-d}^{inv} & G_{ci-q}^{inv} \\ G_{io-d}^{inv} & -Y_{o-d}^{inv} & G_{cr-qd}^{inv} & G_{co-d}^{inv} & G_{co-qd}^{inv} \\ G_{io-q}^{inv} & G_{cr-dq}^{inv} & -Y_{o-q}^{inv} & G_{co-dq}^{inv} & G_{co-q}^{inv} \end{bmatrix} \begin{bmatrix} \hat{i}_{in}^{inv} \\ \hat{v}_{o-d}^{inv} \\ \hat{v}_{o-q}^{inv} \\ \hat{d}_d^{inv} \\ \hat{d}_q^{inv} \end{bmatrix}, \quad (8)$$

where the 3×5 matrix consists of the transfer functions between the input and output variables and the ac-variables are represented in the synchronously rotating *dq*-reference frame. The derivation of these transfer functions can be found, for example in [11].

The inverter is controlled using a cascaded control scheme: the output current *d*-component control acts as the inner loop and its reference is defined by the dc-link voltage controller. A PI controller is adopted in this paper due to its simple structure and easy implementation utilising the *dq*-reference frame. The control system is illustrated in Fig. 4.

2.4 Integrating the effect of BC and PVG into the inverter dynamic model

Based on (8), the linear small-signal model of the inverter at an open loop can be depicted as inside the dashed area in Fig. 5 (as a un-terminated model, without the load effect). The non-ideal characteristics of the PVG, i.e. the dynamic resistance, can be presented using an admittance term

$$Y_{pv} = \frac{1}{r_{pv}} \quad (9)$$

in parallel with the current source. That is, the PVG (output) current can be given as

$$i_{link}^{pv} = i_{in}^{pv} - Y_{pv} v_{pv}, \quad (10)$$

where the voltage over the PVG v_{pv} equals to the dc-link voltage. Based on (4) and (10), the PVG and BESS can be included as in the rest of Fig. 5 thus representing the linear equivalent circuit for the whole system: the three-phase one-stage PV inverter with the BC connected at the dc link and operated with battery current control. The controlled variables are the battery current, the voltage over the PVG, i.e. the dc-link voltage, and the inverter output current.

As can be concluded from the figure, the effect of the BC and the PVG on the inverter dynamics can be analysed by inserting the BC and PVG small-signal dynamic models into the small-signal dynamic model of the inverter. More precisely, by following Kirchhoff's current law, the inverter input current is substituted with the sum of the PVG (output) current and the BC output current as in (11), thus, taking the effect of these two sources into account.

$$\hat{i}_{in}^{inv} = \hat{i}_{link}^{bc} + \hat{i}_{pv} \quad (11)$$

By presenting the inverter dynamics as in (8) and the BC closed-loop dynamics as in (4) and then following the approach, the BC and PVG -affected inverter dynamics can be given by (14). From these transfer functions, the effect of the BC and the PVG can be concluded. Thus, for example the source-affected control-related transfer functions of the inverter can be given as

$$G_{ci-d}^{inv-S} = \frac{G_{ci-d}^{inv}}{1 + Z_{in}^{inv} Y_o^S}, \quad (12)$$

$$G_{co-d}^{inv-S} = G_{co-d}^{inv} - \frac{G_{io-d}^{inv} G_{ci-d}^{inv} Y_o^S}{1 + Z_{in}^{inv} Y_o^S}. \quad (13)$$

Therefore, the effect of the PVG and the BC on the inverter control dynamics can be predicted based on these equations by estimating their output admittances, i.e. the dynamic behaviour between the dc-link voltage and the current fed/drawn to/from the dc link.

3 Small-signal stability analysis

By following the stated approach, the frequency responses can be evaluated for different system parameters. The small-signal stability of the chosen system can be analysed using the derived transfer functions and Bode or Nyquist plots under different operating conditions. In line with the notation in Fig. 1, the used parameters are given in Table 1.

3.1 Control loop gains

Fig. 6–8 present the source-affected inverter control-to-output current *d*-component frequency responses when the BC is operated in open- and closed-loop in discharging mode and when it is disconnected, i.e. the PVG is the only source taken into account. Changing the BC mode to charging does not change the results significantly, so they are left out of the paper. The solid black lines

Table 1 Parameter values used in the analysis

Parameter	Value	Parameter	Value
C_{dc}	1 mF	C_b	1 μF
L	1 mH	L_b	1.3 mH
f_{grid}	60 Hz	v_{batt}	200 V
v_{dc}	350…550 V	i_{batt}	± 5 A
MPP	480 V, 8 A (STC)	f_{sw}	20 kHz

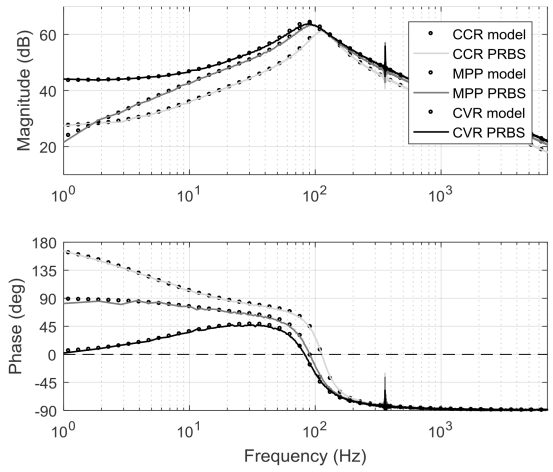

Fig. 6 *Frequency response of G_{co-d}^{inv-S} when BC is disconnected*

represent the frequency responses measured from MATLAB-Simulink model when the PVG is operated in CVR, the grey solid lines at MPP, and the light grey solid lines in CCR. The dotted lines represent the corresponding predicted frequency responses based on the derived model, i.e. Equation (13). It is clear, that in all the considered modes the model predicts the frequency response with good accuracy.

When the PVG is operated in CCR and the BC is disconnected, the control-to-*d*-channel current transfer function includes a low-frequency right-half-plane (RHP) zero that increases the phase at low frequencies to 180° instead of 0° (as when the PVG is operated in CVR). This can be seen in Fig. 6. Since the inverter is operated using a cascaded control scheme in which the outer loop controls the dc-link voltage and the inner loop the inverter current, the RHP zero becomes an RHP pole in the dc-voltage control loop.

The dc-voltage control is usually tuned for a low bandwidth due to the limitations set by the cascaded control scheme and to mitigate second harmonic ripple caused by un-balanced grid voltages. As a rule of thumb, the crossover frequency of the control loop gain should be at least two times higher than the frequency of the RHP-pole [12]. As a result, the low-frequency RHP-pole can easily cause instability. It should also be noted that the frequency of the RHP-pole also depends on the value of the dc-link capacitance and the controller tuning.

However, when the PVG is operated in CCR and the BC is added to the system and operated in closed-loop, its output admittance shifts the RHP zero to a lower frequency. This can be seen in the figures by comparing Fig. 6 with Fig. 7: at low frequencies, the phase of G_{co-d}^{inv-S} is lower when the BC is used. Due to the lower frequency of the RHP zero, the inverter dc-voltage control is less likely to become unstable. This allows a more flexible control design. Therefore, the introduction of BC has a positive effect on the inverter's stability.

Furthermore, when the BC is operated in open-loop, there exists no RHP zero in the inverter control-to-output current *d*-component transfer function, because the BC output admittance shifts the RHP zero to the LHP (left-half-plane) (see (14)) side. Consequently, in Fig. 8, the phase of the frequency response in CCR starts at 0° at low frequencies. Therefore, the RHP pole does not limit the dc-voltage control bandwidth and it can be chosen more freely. However, due to batteries' sensitivity to over-current and over-charge, open-loop control cannot be used.

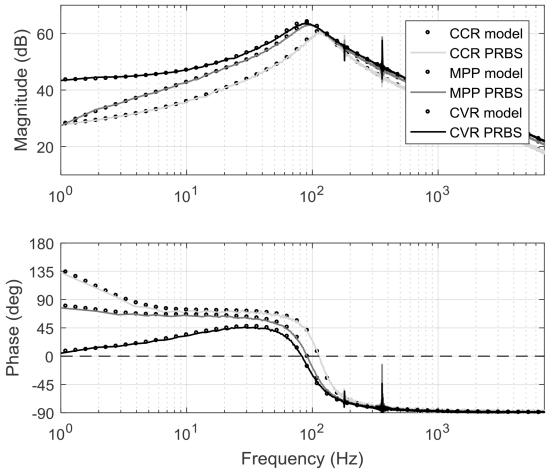

Fig. 7 *Frequency response of G_{co-d}^{inv-S} when BC is discharged in closed-loop (5 A)*

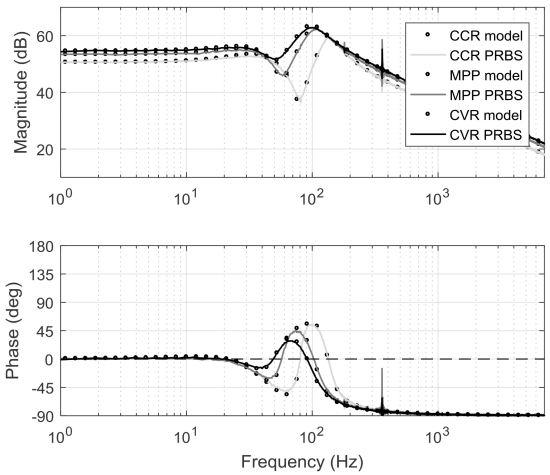

Fig. 8 *Frequency response of G_{co-d}^{inv-S} when BC is discharged in open loop (5 A)*

3.2 Root-loci analysis

In this section, root-loci plots of the real zero of the source-affected inverter control-to-output current *d*-component transfer function (i.e. G_{co-d}^{inv-S}) under a wide range of PVG voltage is analysed. The focus is only on this zero to simplify the results and to further investigate its effect on the inverter control dynamics.

Fig. 9 presents the location of the zero in the s-plane of the Laplace transform, where the parameter s represents the complex angular frequency, at different PVG voltages. As the PVG voltage increases, the zero moves along the real axis from 10.7 to −16.0 rad/s when the BESS is discharged, from 28.5 to −56.1 rad/s when the BESS is disconnected, and from 10.6 to −15.9 rad/s when the BESS is charged. In all the cases, when the PVG is operated at the MPP voltage, the zero is at the origin. However, when the PVG is operated in the CCR, the BESS limits the frequency of the RHP zero to lower frequencies (both in charging and discharging modes) compared to the situation where the BESS is disconnected.

4 Time-domain simulation results

In this section, the effect of the RHP pole in the dc-link control loop on the system stability is demonstrated in time-domain using a MATLAB-Simulink simulation. The results are shown in Fig. 10, where the dc-link voltage is controlled at 300 V so that the PVG operates in CCR, thus introducing the RHP pole in the control dynamics. The dc-voltage controller is tuned with a cross-over frequency of 10 Hz, i.e. 62.8 rad/s. When the BC is connected, the RHP pole is at a frequency of 9.2 rad/s, thus enabling a stable control.

$$\begin{bmatrix} \hat{v}_{\mathrm{in}}^{\mathrm{inv}} \\ \hat{i}_{\mathrm{o-d}}^{\mathrm{inv}} \\ \hat{i}_{\mathrm{o-q}}^{\mathrm{inv}} \end{bmatrix} = \frac{1}{\sigma} \begin{bmatrix} Z_{\mathrm{in}}^{\mathrm{inv}} & G_{\mathrm{io-c}}^{\mathrm{inv}} Z_{\mathrm{in}}^{\mathrm{inv}} & T_{\mathrm{oi-d}}^{\mathrm{inv}} & T_{\mathrm{oi-q}}^{\mathrm{inv}} \\ G_{\mathrm{io-d}}^{\mathrm{inv}} & G_{\mathrm{io-c}}^{\mathrm{bc}} G_{\mathrm{io-d}}^{\mathrm{inv}} & -\left(Y_{\mathrm{o-d}}^{\mathrm{inv}}\sigma + G_{\mathrm{io-d}}^{\mathrm{inv}} T_{\mathrm{oi-d}}^{\mathrm{inv}} Y_{\mathrm{o}}^{\mathrm{S}}\right) & -\left(Y_{\mathrm{o-qd}}^{\mathrm{inv}}\sigma + G_{\mathrm{io-d}}^{\mathrm{inv}} T_{\mathrm{oi-q}}^{\mathrm{inv}} Y_{\mathrm{o}}^{\mathrm{S}}\right) \\ G_{\mathrm{io-q}}^{\mathrm{inv}} & G_{\mathrm{io-c}}^{\mathrm{bc}} G_{\mathrm{io-q}}^{\mathrm{inv}} & -\left(Y_{\mathrm{o-dq}}^{\mathrm{inv}}\sigma + G_{\mathrm{io-q}}^{\mathrm{inv}} T_{\mathrm{oi-d}}^{\mathrm{inv}} Y_{\mathrm{o}}^{\mathrm{S}}\right) & -\left(Y_{\mathrm{o-q}}^{\mathrm{inv}}\sigma + G_{\mathrm{io-q}}^{\mathrm{inv}} T_{\mathrm{oi-q}}^{\mathrm{inv}} Y_{\mathrm{o}}^{\mathrm{S}}\right) \end{bmatrix}$$

$$\begin{bmatrix} G_{\mathrm{ci-d}}^{\mathrm{inv}} & G_{\mathrm{ci-q}}^{\mathrm{inv}} \\ G_{\mathrm{co-d}}^{\mathrm{inv}}\sigma - G_{\mathrm{io-d}}^{\mathrm{inv}} G_{\mathrm{ci-d}}^{\mathrm{inv}} Y_{\mathrm{o}}^{\mathrm{S}} & G_{\mathrm{co-qd}}^{\mathrm{inv}}\sigma - G_{\mathrm{io-d}}^{\mathrm{inv}} G_{\mathrm{ci-q}}^{\mathrm{inv}} Y_{\mathrm{o}}^{\mathrm{S}} \\ G_{\mathrm{co-dq}}^{\mathrm{inv}}\sigma - G_{\mathrm{io-q}}^{\mathrm{inv}} G_{\mathrm{ci-d}}^{\mathrm{inv}} Y_{\mathrm{o}}^{\mathrm{S}} & G_{\mathrm{co-q}}^{\mathrm{inv}}\sigma - G_{\mathrm{io-q}}^{\mathrm{inv}} G_{\mathrm{ci-q}}^{\mathrm{inv}} Y_{\mathrm{o}}^{\mathrm{S}} \end{bmatrix} \begin{bmatrix} \hat{i}_{\mathrm{in}}^{\mathrm{pv}} \\ \hat{v}_{\mathrm{batt}}^{\mathrm{bc}} \\ \hat{v}_{\mathrm{o-d}}^{\mathrm{inv}} \\ \hat{v}_{\mathrm{o-q}}^{\mathrm{inv}} \\ \hat{d}_{\mathrm{d}}^{\mathrm{inv}} \\ \hat{d}_{\mathrm{q}}^{\mathrm{inv}} \end{bmatrix} \tag{14}$$

$$Y_{\mathrm{o}}^{\mathrm{S}} = Y_{\mathrm{pv}} + Y_{\mathrm{o-c}}^{bc}, \quad \sigma = 1 + Z_{\mathrm{in}}^{\mathrm{inv}} Y_{\mathrm{o}}^{\mathrm{S}}$$

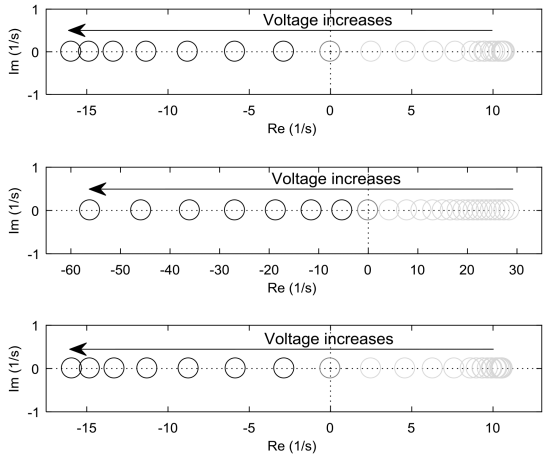

Fig. 9 *Low-frequency zero of* $G_{\mathrm{co-d}}^{\mathrm{inv-S}}$ *on the real-axis for different PVG voltages when the BESS is*
(a) Discharging ***(b)*** Disconnected and, ***(c)*** Charging

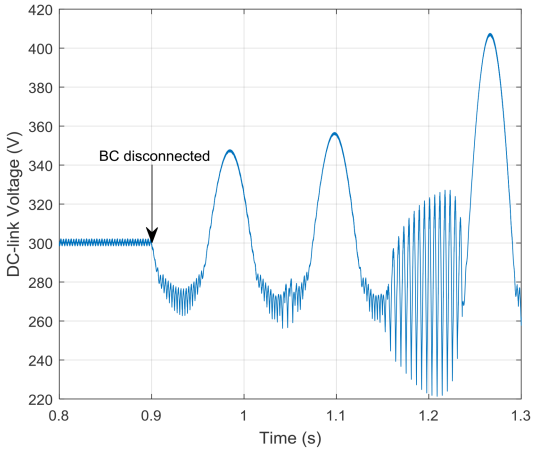

Fig. 10 *Dc-link voltage before and after the BC is disconnected while the PVG is operated in CCR*

However, at 0.9 s, the BC is disconnected from the system, and the RHP pole shifts to 28.5 rad/s, making the system unstable. This can be clearly seen in the figure as the increasing oscillation in the dc-link voltage. Due to the cascaded control loop, also the output current starts to oscillate increasingly. This instability can be predicted using the derived transfer functions to study the voltage control loop, which indicates a negative phase margin when the system is unstable.

5 Conclusion

This paper presents a method to solve the dynamic model of a grid-connected photovoltaic inverter with battery storage, thus predicting accurately, for example, the inverter's control-related transfer functions and the system's output impedance. Note, that the used method can also be applied to any type of inverter, sources, and different control schemes. The derived model has been verified through simulation studies in both time and frequency domains in all the operating modes. Using the model, the effect of PVG and the BC on the dynamics of the grid-connected inverter has been analysed.

The analysis shows that the BC has a significant positive effect on the inverter performance, and more precisely, on the dc-link voltage control, thus preventing instability arising in the CCR of the PVG. In the closed-loop operating mode, the BC operates as a constant-power source and its output admittance moves the characteristic low-frequency RHP pole of the dc-link voltage control towards the origin compared to a situation where the BC is disconnected. Consequently, either the dc-link capacitor can be selected to be smaller or more flexibility is allowed when designing the bandwidth of the dc-link voltage controller without compromising the stability of the system.

6 References

[1] Nosair, H., Bouffard, F.: 'Flexibility envelopes for power system operational planning', *IEEE Trans. Sustain. Energy*, 2015, **6**, (3), pp. 800–809

[2] Soder, L., Abildgaard, H., Estanqueiro, A., *et al.*: 'Experience and challenges with short-term balancing in European systems with large share of wind power', *IEEE Trans. Sustain. Energy*, 2012, **3**, (4), pp. 853–861

[3] Zhai, Q., Meng, K., Dong, Z.Y., *et al.*: 'Modeling and analysis of lithium battery operations in spot and frequency regulation service markets in Australia electricity market', *IEEE Trans. Ind. Inf.*, 2017, **13**, (5), pp. 2576–2586

[4] Savkin, A.V., Khalid, M., Agelidis, V.G.: 'A constrained monotonic charging/discharging strategy for optimal capacity of battery energy storage supporting wind farms', *IEEE Trans. Sustain. Energy*, 2016, **7**, (3), pp. 1224–1231

[5] Li, X., Hui, D., Lai, X.: 'Battery energy storage station (BESS)-based smoothing control of photovoltaic (PV) and wind power generation fluctuations', *IEEE Trans. Sustain. Energy*, 2013, **4**, (2), pp. 464–473

[6] Tan, X., Wu, Y., Tsang, D.H.K.: 'Pareto optimal operation of distributed battery energy storage systems for energy arbitrage under dynamic pricing', *IEEE Trans. Parallel Distrib. Syst.*, 2016, **27**, (7), pp. 2103–2115

[7] Nousiainen, L., Puukko, J., Mäki, A., *et al.*: 'Photovoltaic generator as an input source for power electronic converters', *IEEE Trans. Power Electron.*, 2013, **28**, (6), pp. 3028–3038

[8] Narasimharaju, B.L., Dubey, S.P., Singh, S.P., *et al.*: 'Modelling and stability analysis of coupled inductor bidirectional DC-DC converter'. 2010 IEEE Int. Conf. of Electron Devices and Solid-State Circuits (EDSSC), Hong Kong, 2010

[9] Ramadan, H.A., Imamura, Y., Yang, S., *et al.*: 'A new stability assessment criterion for dc power systems using multi-level virtual conductors'. 2014 IEEE 15th Workshop on Control and Modeling for Power Electronics (COMPEL), Santander, 2014

[10] Liu, S., Dougal, R.A.: 'Dynamic multiphysics model for solar array', *IEEE Trans. Energy Convers.*, 2002, **17**, (2), pp. 285–294

[11] Messo, T., Jokipii, J., Puukko, J., *et al.*: 'Determining the value of DC-link capacitance to ensure stable operation of a three-phase photovoltaic inverter', *IEEE Trans. Power Electron.*, 2014, **29**, (2), pp. 665–673

[12] Skogestad, S., Postlethwaite, I.: '*Multivariable feedback control: analysis and Design*' (John Wiley & Sons Ltd., West Sussex, England, 1996)